

A parametric study of the generation and degeneration of wind-forced long internal waves in narrow lakes

TAKAHIRO SAKAI† AND L. G. REDEKOPP

Department of Aerospace & Mechanical Engineering, University of Southern California, Los Angeles, CA 90089-1191, USA

(Received 11 February 2009; revised 13 October 2009; accepted 14 October 2009;
first published online 4 February 2010)

The generation and energy downscaling of wind-forced long internal waves in strongly stratified small-to-medium sized narrow lakes are studied. A two-layer nonlinear model with forcing and damping is employed. Even though the wave field is fundamentally bidirectional in nature, a domain folding technique is employed to simulate the leading-order internal wave field in terms of a weakly nonlinear weakly dispersive model equation of Korteweg–deVries type. Parametric effects of wind-forcing and environmental conditions, including variable topography and variable basin width, are examined. Energy downscaling from basin-scale waves to shorter scales are quantified by means of a time evolution of the wave energy spectra. It is demonstrated that an internal wave resonance is possible when repetitive wind-forcing events arise with a frequency near the linear seiche frequency. An attempt is made to apply the model to describe the shoaling of long waves on sloping endwall boundaries. Modelling of the energy loss and energy reflection during a shoaling event is calibrated against laboratory experiments.

1. Introduction

Hydrodynamic motion in the interior of lakes is crucial to issues such as water quality and ecological sustainability. The interior dynamics is energized primarily by wind action, with the deposition of energy into basin-scale motions through a transfer of the wind stress across the free surface boundary layer. In typical stably stratified lakes the action of a surface wind stress drives not only high-frequency surface waves, whose region of influence is mostly confined to the upper-mixed layer, but also forces through volumetric transport in the closed basin a significant tilting of the internal density field, inducing a basin-scale pressure gradient. Then, when the wind stress subsequently diminishes, the unbalanced large-scale horizontal pressure gradient relaxes through a dynamic process leading to the appearance of a spectrum of internal waves whose state at any subsequent time determines, and dominates, the internal weather of a closed basin. The consequent internal wave field contains, in general, energy in scales ranging from basin scale to those on the order of the mixed-layer depth, and in frequencies ranging from the seiche period up to the buoyancy frequency (Saggio & Imberger 1998). Motions encompassing this wide range of scales are generally propagative, possess three dimensional features and can effectively transfer

† Email address for correspondence: tsakai@usc.edu

momentum and kinetic energy throughout the basin and to boundary domains where the energy is principally dissipated (Imberger 1994). Hence, internal waves serve as energy distributors and assert a pivotal role in driving transport and mixing processes in lakes, and they define the flux path of biological and chemical particles within a basin (Imberger 1998). Understanding the principal mechanisms whereby bio-geochemical transport occurs in a basin is crucial to establishing management procedures and remediation policies for vulnerable and fragile fresh water resources.

For small to medium sized lakes, particularly narrow lakes where the effect of the earth's rotation is negligible, a wind blowing over the surface induces a downwind transport in the epilimnion. The result in a closed basin is an accumulation of epilimnion water near the leeward shore with a consequent excess of hypolimnion water at the windward end due to volume conservation. There is an attendant, but very slight, upslope tilt of the free surface, but the downslope tilt in the metalimnion in the wind direction is much more pronounced (Mortimer 1952; Monismith 1986; Stevens & Imberger 1996). If the wind is sustained for a significant fraction of the internal pendulum (alt. seiche) period, and then relaxes, the unbalanced baroclinic pressure gradient causes the tilted thermocline to tend to return to equilibrium. This return to equilibrium occurs, initially at least, through formation of a basin-scale internal seiche. Although a barotropic seiche also emerges over the free surface, the basin-scale internal seiche is far more energetic (cf. Heaps & Ramsbottom 1966; Heaps 1984). The energy deposited into wind-generated basin-scale internal motion is eventually transformed through a downscale cascade of energy. This energy transfer occurs across the spectrum of internal waves into small-scale turbulence and other dissipative motions over the full extent of the basin boundaries. The dominant part of the energy is dissipated by turbulent mixing in the bottom boundary under long internal waves and by the breaking and interaction of internal waves at sloping, shore-line boundaries (Michallet & Ivey 1999). A much smaller fraction of the energy is dissipated by turbulent mixing which is driven by wave-induced shear instability in the interior of the basin. These mixing and dissipation processes, as well as the turbulent mixing process in the upper surface layer, are an important and active area of research (see review by Wüest & Lorke 2003).

Field observations in Lake Biwa by Saggio & Imberger (1998) suggest that the decay of internal wave energy is much faster than predicted by estimates based on any typical internal dissipation rate. They also suggest that the shorter scale higher frequency waves trapped in the metalimnion seem to distribute the energy and reshape the internal energy spectrum. Generation and dissipation of such high-frequency waves are yet to be identified. Thorpe *et al.* (1996) discussed potential sources of the high-frequency waves, listing such possibilities as: (i) nonlinear steepening of the basin-scale waves leading to the appearance of a packet of internal solitary waves (ISWs); (ii) the thermocline jump propagating around local irregular and rough bathymetry generates local disturbances which radiate internal waves and (iii) a region of strong shear with low Richardson number generated across the thermocline as long waves propagate, generating locally-unstable patches with radiating internal waves.

An accumulating body of field observations has clearly revealed the existence of the internal seiche and its frequent degeneration into a steep nonlinear wavefront. Furthermore, this body of observations has provided firm evidence of packets of propagating ISWs wherein a higher frequency dynamics is present (e.g. Thorpe & Hall 1972; Hunkins & Fliegel 1973; Farmer 1978; Wiegand & Carmack 1986). Laboratory experiments (Horn, Imberger & Ivey 2001) have elucidated the steepening of the initial seiche into a nonlinear front, along with its subsequent evolution into packets

of bidirectionally propagating long waves. These long-wave packets seem to exhibit a dominant balance between nonlinearity and non-hydrostatic (dispersive) effects, the balance underlying the existence of permanent features such as solitary waves (Grimshaw 2002). Laboratory experiments have also elucidated processes associated with the shoaling and reflecting of ISWs at a sloping boundary. Shoaling ISWs are found to break and dissipate a substantial fraction of their energy due to turbulent mixing, but a non-trivial reflection in terms of a transformed packet occurs (Helfrich 1992; Michallet & Ivey 1999; Boegman, Ivey & Imberger 2005a; Bourgault & Kelly 2007; Lamb & Nguyen 2009). Generation of nonlinear long-wave packets (nominal ISWs) following the early steepening of the initial basin-scale tilt is, therefore, one of the very important pathways for energy downscaling. Nonlinear steepening and generation of ISWs are, however, strongly dependent on the strength and spatio-temporal distribution of the applied wind stress, and also on the background environment (stratification and bathymetry).

The functional dependence of the energy deposition into the internal wave spectrum, and the evolution of the spectrum, on the multiple parameters of the problem is not well understood. Horn *et al.* (2001) studied the degeneration of a basin-scale seiche into higher frequency solitary waves for a range of wind-driven tilts and background environments by using a laboratory model. Boegman, Ivey & Imberger (2005b) described the energetics of a basin-scale seiche, its consequent nonlinear surge, and its later evolution in frequency space by using the same laboratory model. They also conducted experiments with a sloping boundary and characterized the energy loss of ISW packets in terms of reflection coefficients and the frequency spectrum (Boegman *et al.* 2005a). Several field observations were also examined by these authors. From a numerical point of view, however, there is a dearth of models that admit a means for rapid exploration of parametric effects on the energetics and dynamics of the internal weather in closed basins. There are two principal reasons for this state of affairs in lake hydrodynamics: (i) most numerical models are based on the hydrostatic approximation and therefore cannot capture the non-hydrostatic effects essential to front evolution and energy downscaling; and (ii) ISWs in numerical models of many lakes lie in subgrid scales, and practical methods for modelling and parameterizations of generation and dissipation of such subgrid scale waves is yet to be developed (e.g. Boegman, Ivey & Imberger 2004). Hence, further understanding of the generation, evolution and dissipation of long-wave features in closed basins (e.g. ISWs), especially the understanding of parametric effects via a rapid-simulation tool, can go a long way towards facilitating the development of reliable and useful numerical models of the broad range of scales associated with wind-driven lake hydrodynamics.

In this report we quantify the downscale energy process of internal waves from the basin scale to scales which are of order 5–10 times the controlling fluid depth (typically the upper-mixed-layer depth). Our approach is to use a simplified theoretical model which includes variable environmental and forcing parameters. The vertical structure is taken in a most simplified form, a two-layer model, and the effect of the earth's rotation is neglected as the model is restricted to high-aspect ratio basins (i.e. the length-to-width ratio is large). These simplifications are advantageous to construction of a simulation model that captures leading-order nonlinear and dispersive effects, and yet allows rapid simulation to reasonably explore a considerable range of parameter settings for various wind-forcing scenarios. In §2 we describe a driven-damped variable-environmental higher order Korteweg–deVries (KdV) model applicable to describing bidirectional propagation of internal waves which are long relative to the controlling depth (i.e. the mixed-layer depth) in a confined basin.

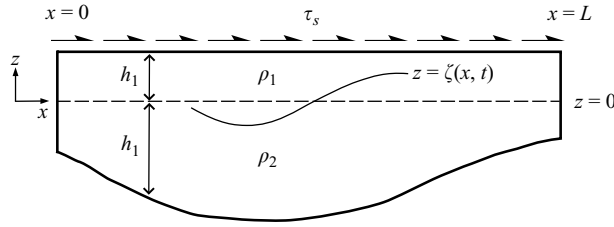


FIGURE 1. Two-layer density stratified lake model.

In §4 we apply the model to a rectangular lake for different wind stress distributions, demonstrate internal wave resonance under periodic wind forcing, and apply the model to various background environments and wind-forcing strengths. In §5 we discuss the downscale energy transfer in lakes by use of a spatio-temporal energy spectrum obtained from model simulations. In §6 the model is applied to lakes with variable topography and width. In §7 we also attempt to extend the model to the case of a sloping endwall and calibrate the simulation model against results from laboratory experiments by Boegman *et al.* (2005a).

2. Evolution model

We consider a lake of length L having a stable two-layer density stratification as depicted in figure 1. The length of the lake, and particularly its width, is assumed to be sufficiently small so that the effect of the earth's rotation is negligible. The upper layer with density ρ_1 and thickness h_1 overlies the heavier lower layer with density ρ_2 and variable thickness $h_2(x)$. If the metalimnion (thermocline) of a stratified lake is sufficiently thin, a two-layer model can be used to rationally approximate the lowest mode dynamics. Such a model, of course, precludes any leakage of energy into higher vertical modes, an effect that almost surely is an important element in the energy transfer to shorter scales in a closed basin, especially for waves propagating through horizontal contractions and undergoing 'reflections' from sloping endwalls. Such effects will be addressed in a subsequent study where coupled-mode evolution equations are derived and simulated (Sakai & Redekopp 2009).

The internal wave motion in this two-layer interfacial model is marked by an interfacial displacement $z = \zeta(x, t)$ from the equilibrium level. The lake is assumed to have a variable width (i.e. variable layer widths $W_1(x)$ and $W_2(x)$ representing the average widths of the respective layers), but its average measure is always assumed to be narrow compared to the length L . In this limit a lateral averaging process can be employed to obtain a laterally averaged value for the dependent variables such as $\zeta(x, t)$. As the density ratio ρ_1/ρ_∞ across the free surface is large compared to the internal density ratio ρ_1/ρ_2 , the upper surface is assumed to be flat, a condition that filters out any surface wave motion. We do allow for the existence of a surface stress $\tau_s(x, t)$, however, to capture the effect of an applied wind stress and its potential for forcing internal wave motions.

Since the propagation space (x direction) is bounded, it is essential to allow a full bidirectionality in any asymptotic approximation of the forced, long-wave dynamics. To this end, a long-wave evolution equation of Boussinesq form is required. However, as shown by Horn *et al.* (2002), the leading-order contribution of bidirectional propagation can be accounted for by use of an extended-folded-domain representation of the unbiased second-order in time Boussinesq model resulting in a first-order in

time KdV model. The asymptotic methodology underlying the rational derivation of such a model equation is quite standard, and the reader can find relevant details in Horn *et al.* (2002). Extending that work to propagation along a variable-width channel using an adaptation of a cross-channel (lateral) averaging procedure employed in earlier work by Teng & Wu (1992), the following evolution model is obtained:

$$\begin{aligned} \zeta_t + c_0 \zeta_x + \frac{c_0}{2} \left\{ \frac{d \ln c_0}{dx} + \frac{d \ln W}{dx} \right\} \zeta + \frac{3}{2} \alpha c_0 \zeta \zeta_x + \alpha_2 c_0 \zeta^2 \zeta_x + \frac{\beta}{2} c_0 \zeta_{xxx} \\ = -\frac{k_b c_0}{2h_2^2} C_f \zeta |\zeta(x, t) - \zeta(2L - x, t)| - \frac{k_s u_{*0}^2}{4c_0} \Phi(x, t), \end{aligned} \quad (2.1)$$

where coefficients are defined by the relations

$$\left. \begin{aligned} c_0^2 &= \frac{(\rho_2 - \rho_1)gh_1h_2}{\rho_1h_2 + \rho_2h_1}, & \alpha &= \frac{\rho_2h_1^2 - \rho_1h_2^2}{(\rho_1h_2 + \rho_2h_1)h_1h_2}, \\ \alpha_2 &= \frac{3}{h_1^2h_2^2} \left[\frac{7}{8} \left(\frac{\rho_2h_1^2 - \rho_1h_2^2}{\rho_1h_2 + \rho_2h_1} \right)^2 - \frac{\rho_2h_1^3 + \rho_1h_2^3}{\rho_1h_2 + \rho_2h_1} \right], \\ \beta &= \frac{h_1h_2}{3} \left(\frac{\rho_1h_1 + \rho_2h_2}{\rho_1h_2 + \rho_2h_1} \right), & k_s &= \frac{\rho_1h_2}{\rho_1h_2 + \rho_2h_1}, & k_b &= \frac{\rho_2h_1}{\rho_1h_2 + \rho_2h_1}. \end{aligned} \right\} \quad (2.2)$$

In this extended forced-dissipative (KdV) model, the effect of variable depth $h_2(x)$ is accounted for through spatially varying coefficients, especially the variable long-wave phase speed $c_0(x)$ and its derivative. The effect of variable lake width is contained in the term involving a single depth-averaged width function $W(x)$. The variable-depth and variable-width effects are included in the derivation of the underlying Boussinesq system, and as such capture naturally the effects of geometric steepening and dispersion. The terms on the right-hand side, respectively, represent the effect of turbulent bottom friction through use of a dimensionless friction coefficient C_f and the effect of a varying surface wind stress described by the function $\Phi(x, t)$. It should be also noted that inclusion of a cubic nonlinear term, yielding what is sometimes referred to as the Gardner equation (Gardner 1971), or alternatively, the extended KdV equation, is included in (2.1) in order to account for higher order nonlinearity beyond the quadratic KdV model. The Gardner equation is now widely recognized as a standard model for ISWs, including variable depth (e.g. see reviews by Helfrich & Melville 2006; Grimshaw, Pelinovsky & Talipova 2007). A further extension to account for a fully nonlinear representation of the long-wave phase speed is currently available and, in fact, is described in §7. In most lakes the isopycnal surfaces intersect the bottom topography, which is not accounted in the model (2.1) as the model assumes that the isopycnal surface intersects vertical endwalls. An extension of (2.1) to basins with a sloping endwall is discussed also in §7.

As elucidated in Horn *et al.* (2002), (2.1) is employed in a periodic computational domain $[0, 2L]$ defined via an even extension of the original physical domain $[0, L]$ about $x = L$ (see figure 2a). Then, the physical solution ζ_p is obtained by even-folding of the solution about $x = L$; that is,

$$\zeta_p = \zeta(x, t) + \zeta(2L - x, t). \quad (2.3)$$

In this way (2.1) serves as a first-order model capturing the dominant physical effects of the wind-generated wave field in narrow lakes. The reduction to a first order in

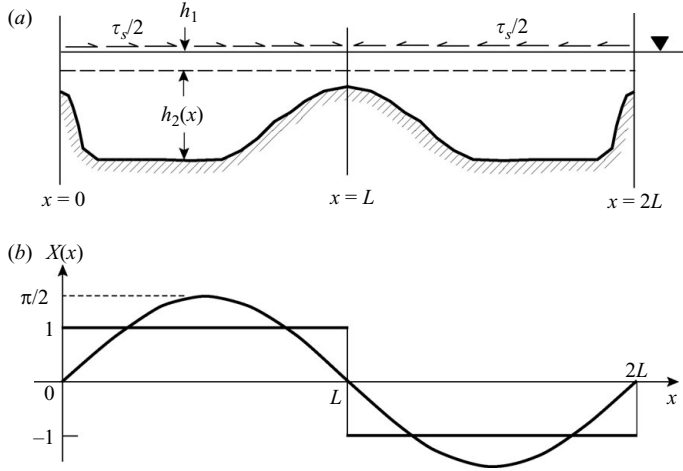


FIGURE 2. (a) Topography is even-extended in the computational domain. The wind stress τ_s is halved and mirrored about $x=L$. Direction of the wind stress in the left and the right half domain are opposite each other. (b) Uniform and sinusoidal wind stress distributions defined in the computational domain.

time dynamical model is a very significant step. Particularly in that it forms the basis for a rapid-integration model useful for exploring the role of different parametric effects in defining the internal wave field set up by wind forcing.

The model defined in (2.1) is presented in dimensional form. In what follows it is useful to recast the equation in dimensionless form. To this end the interface displacement is scaled with the epilimnion depth h_1 , the propagation coordinate x is scaled with the basin length L and time is scaled with the nominal internal seiche period $2L/c_{00}$, where c_{00} is the long-wave phase speed computed using a base value of the lower layer depth h_{20} . Furthermore, the wind stress function $\Phi(x, t)$ is scaled with the square of a reference friction velocity u_{*0}^2 . Using these scales, (2.1) takes the non-dimensional form

$$f_t + 2c_0 f_x + 3\alpha c_0 f f_x + 2\alpha_2 c_0 f^2 f_x + \left(\frac{h_1}{L}\right)^2 \beta c_0 f_{xxx} + c_0 \left\{ \frac{d \ln c_0}{dx} + \frac{d \ln W}{dx} \right\} f = -k_b \frac{L}{h_1} \left(\frac{h_1}{h_2}\right)^2 C_f f |f(x, t) - f(2-x, t)| - \frac{1}{2} k_s \mathcal{W}^{-1} X(x) T(t). \quad (2.4)$$

The coefficients c_0 , α , α_2 , β , k_b and k_s are now recast in dimensionless form, the dependent variable $f(x, t)$ is simply ζ/h_1 , and (x, t) are dimensionless space–time coordinates scaled with their appropriate reference values. The corresponding physical solution given in (2.3) is now denoted as $f_p (= \zeta_p/h_1)$. The wind stress distribution function $\Phi(x, t)$ has been separated into a dimensionless spatial part $X(x)$ and a dimensionless temporal part $T(t)$, and the use of non-dimensional variables has introduced the Wedderburn number \mathcal{W} (cf. Imberger & Patterson 1990 and Horn *et al.* 2001). It is defined by

$$\mathcal{W} = \frac{c_{00}^2 h_1}{u_{*0}^2 L}. \quad (2.5)$$

The Wedderburn number is useful for parameterizing the strength of the wind stress and, with reference to (2.1), measures the magnitude of the baroclinic pressure gradient ($c_0 \zeta_x \sim c_{00} h_1 / L$) relative to the vertical gradient of the wind stress ($\sim u_{*0}^2 / c_{00}$).

3. Numerical method

To simulate the model described by (2.4) we employ the pseudo-spectral method similar to that in Fornberg & Whitham (1978). Since the spatio-temporal model equation is integrated in the spatially periodic computational domain, the spatial derivatives can be computed accurately and efficiently by using the fast Fourier transform. The third-order multi-step scheme is used for time integration. The computer program MKDV, in which these numerical methods are implemented, was originally developed by Horn *et al.* for simulating the initial value problem for a two-layer model for a rectangular lake. It has been shown in their work that the simulation results using MKDV agree qualitatively with their laboratory experiments (Horn *et al.* 2002). The program was modified to accommodate the introduction of applied wind forcing and a benthic (turbulent) friction in order to meet the objectives of this study. The simulation results presented here used a total of $N_x = 1024$ spatial mesh points in the computational domain $[0, 2]$ and a time step of $\Delta t = 5 \times 10^{-6}$ unless as otherwise noted.

In the specialized limit of a flat bottom and constant width (i.e. homogeneous coefficients), and if the wind-forcing and boundary layer friction terms are absent, the KdV equation possesses infinitely many conserved densities for either a periodic or an unbounded domain (e.g. Drazin & Johnson 1989). In order to validate our modified program, we evaluate the leading three conserved quantities

$$E_1 = \int_0^2 f \, dx; \quad E_2 = \int_0^2 f^2 \, dx; \quad E_3 = \int_0^2 \left\{ \frac{3}{2} \alpha c_0 f^3 + \frac{1}{2} \alpha_2 c_0 f^4 - \frac{3}{2} \beta c_0 f_x^2 \right\} dx \tag{3.1}$$

from simulation results. $f(x, t)$ is a solution to (2.4) in the computational domain $[0, 2]$. Since the resulted computational domain is finite and periodic, these integrations must be evaluated over the computational domain. E_1 represents conservation of mass and E_2 is that of energy including both potential and kinetic energy (see Appendix). These conserved quantities are evaluated for several simulations using different sets of parameters. Figure 3 shows time series of the conserved quantities for one of the typical runs. The physical parameters were chosen as $h_1/h_2 = 1/5$ and $h_1/L = 0.002$ in the simulation. A uniform wind stress with Wedderburn number $\mathcal{W} = 1.0$ is applied for $0 \leq t \leq 1/4$ starting from an initial state with a flat interface at rest (i.e. E_1 is zero theoretically). The calculated value of E_1 is $O(10^{-7})$, which is the order of machine precision (the program was run in single precision arithmetic). The magnitudes of E_2 and E_3 increase until $t = 1/4$ whereupon the wind forcing is discontinued. Thereafter, the latter two conserved densities remain virtually constant, confirming a very respectable simulation fidelity.

4. Effects of environmental parameters

In this section we consider the role of various parametric effects on the wind-generated wave field in a lake devoid of geometric inhomogeneities; that is, in a ‘box’ lake having constant depth and constant width. Referring to the model (2.4), and after invoking the Boussinesq approximation ($\rho_1 \approx \rho_2$), the set of basic control

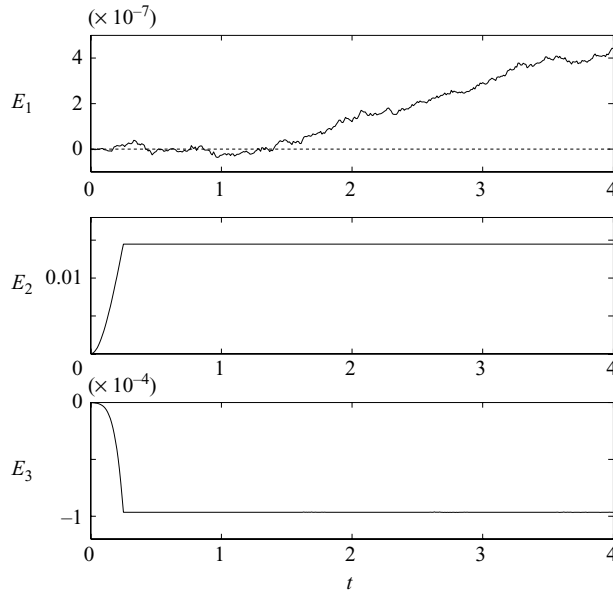


FIGURE 3. Time series of the conserved quantities E_1 , E_2 and E_3 .

parameters are reduced to h_1/L , h_1/h_2 , C_f and \mathcal{W} . For most of the results that follow a fixed friction coefficient $C_f = 0.0025$ was used. This value has been recommended in previous studies of frictionally damped, long-wave models of internal wave motions (cf. Baines 1995; Grimshaw 2002). We study here the effects of these parameters on the evolution of the nonlinear wave field driven by wind forcing, and seek to clarify the transfer of internal wave energy from the basin-scale to progressively shorter internal waves.

4.1. Effect of spatial wind stress distribution

The spatial wind stress distribution function $X(x)$ is prescribed arbitrarily provided only that it is antisymmetric about $x=1$ in the extended computational domain $[0, 2]$. This antisymmetry requirement may cause the prescribed distribution $X(x)$ to be discontinuous at both the physical and computational boundaries. Such spatial discontinuities in the forcing tend to produce small-scale numerical oscillations every time step, and they soon pollute the numerical solution. To alleviate these spurious high-wavenumber oscillations, one can introduce an artificial smoothing of the distribution $X(x)$ at the discontinuities. Alternatively, one can apply a spectral (low pass) filtering of the numerical solution after a specified number of time steps while the wind-forcing term is active. Both treatments are effective, but we mainly used the spectral filtering, filtering out the upper 7/8 of the total Fourier modes during the time the wind forcing is active. If the forcing continues for an extensive time (e.g. see §§ 4.3 and 4.5), or if the forcing is relatively strong so that nonlinearity becomes important and ISWs emerge during the time wind forcing is active, the use of spatial stress smoothing is preferred over post spectral filtering.

In this study, we limit the choices for $X(x)$ to several functionally simple distributions: either a uniform distribution, or a sinusoidal distribution, or a linearly varying distribution, and examine the influence of different stress densities. The integral of the stress over the physical surface is taken to be equal in any comparison of lake responses (see figure 2b) to different stress distributions. Figure 4, for example,

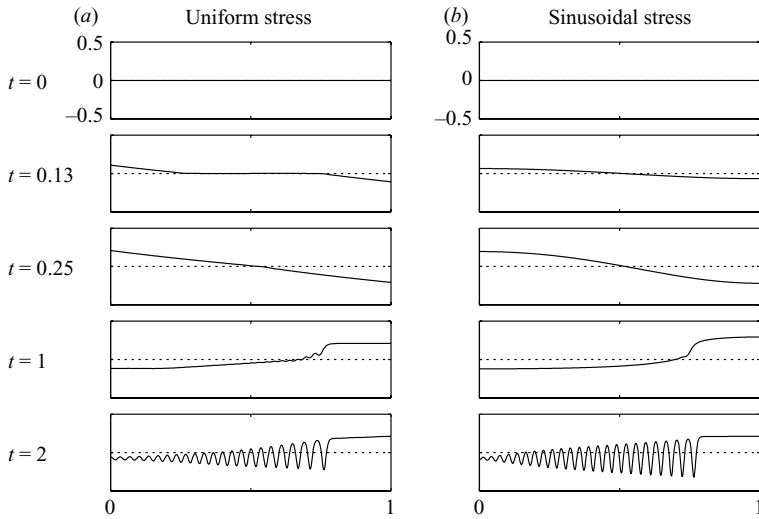


FIGURE 4. Snap shots of the interface displacement f_p for uniform (a) and sinusoidal (b) wind stress distributions. Wind stress blowing to the right with $\mathcal{W} = 1$ is applied for $0 \leq t \leq 1/4$.

compares the simulated wave evolution for a uniform distribution with that of a sinusoidal distribution with the physical parameters $h_1/h_2 = 5$ and $h_1/L = 0.002$. A spatially uniform wind stress with $\mathcal{W} = 1$ is applied continuously for $0 \leq t \leq 1/4$, and is switched off thereafter. The interface, which is uniformly flat initially, is progressively depressed at the leeward end and elevated at the windward end. The depression propagates windward and the elevation propagates leeward. The propagation speed of these interfacial pulses is essentially equal to the linear, long-wave phase speed. At $t = 1/4$ the tilted surface closely approximates a tilted straight line when the stress distribution is uniform, and is smoothly curved when the stress distribution is sinusoidal. After the wind is turned off, the interface begins to oscillate as a standing wave (internal seiche). However, a nonlinear steepening occurs forming a front on the background seiche. This front is gradually steepened ($t = 1$) and, at some later time, nonlinear and dispersive effects become closely balanced allowing the formation of a train of oscillatory waves (ISWs) which gradually disperse throughout the domain ($t = 2$). The wavetrain reflects at boundaries, propagating back and forth in the physical domain. As evident in figure 4, the peak amplitude of waves forced by the sinusoidal stress distribution is relatively larger than that forced by the uniform stress distribution. A wind stress of duration $t = 1/4$ is used as a reference value as it corresponds to the time when the interface is first deformed from its equilibrium position everywhere except at the lake centre. The model includes the boundary loss term, but a decay in the energy is almost imperceptible for the total integration time of the present simulation and for the selected friction coefficient. The time series of the integral E_2 , which is a direct measure of the total energy of the internal wave field forced by the wind (see Appendix), achieves a value of unity for the uniform distribution as compared to a value of $E_2 = 3/2$ for the sinusoidal distribution at $t = 1/4$, even though the integrated stress distributions are identical. The locally higher stress density in the middle of the physical domain for the sinusoidal stress case induces a locally larger pressure gradient and, therefore, drives a locally steeper interface (see figure 4 at $t = 1/4$). Also, such a locally high stress density injects larger

energy solely to the gravest horizontal mode (half Fourier sine wave), resulting in larger energy than that of the uniform stress case (cf. §4.2).

4.2. Effect of Wedderburn number and depth ratio

An estimate of the early distortion of the metalimnion (interface), and the scaling of the energy deposition into the internal wave field by an applied wind stress, can be pursued by use of the linearized non-dispersive frictionless version of (2.1). Supposing an impulsive onset of the wind stress with spatial distribution $X(x)$ written in terms of Fourier series

$$X(x) = \sum_{n=1}^{\infty} B_n \sin\left(\frac{n\pi x}{L}\right), \quad (4.1)$$

representing the antisymmetric stress distribution on the extended interval $[0, 2L]$, one can derive the following relations:

$$f_p(0, t) = \frac{\zeta_p(0, t)}{h_1} = \frac{k_s}{4\pi\mathcal{W}} \sum_{n=1}^{\infty} \frac{B_n}{n} (1 - \cos 2n\pi t); \quad (4.2)$$

$$E_{2p}(t) = \int_0^1 f_p^2(x, t) dx = \frac{1}{8\pi} \left(\frac{k_s}{\mathcal{W}}\right)^2 \sum_{n=1}^{\infty} \left(\frac{B_n}{n}\right)^2 (1 - \cos 2n\pi t)^2. \quad (4.3)$$

If the wind stress is linearly varying along the lake as given by $X(x) = 1 + \delta(1 - 2x)$ where δ is a spatial gradient of the stress, then the sine-transform B_n is given by

$$B_n = \frac{2}{n\pi} \{1 - (-1)^n + \delta(3 - (-1)^n)\}. \quad (4.4)$$

It is worth noting that the quantity k_s/\mathcal{W} in (4.2) and (4.3) can, in the Boussinesq approximation, be replaced by \mathcal{W}_*^{-1} where \mathcal{W}_* is the Wedderburn number defined in terms of the reference phase speed $c_{0*} = \sqrt{\tilde{g}h_1}$ as opposed to the true phase speed c_{00} .

Our simulations of the model (2.4) reveal that the energy scaling given by (4.3) yields excellent results over a range of moderate Wedderburn numbers (e.g. $0.5 \leq \mathcal{W} \leq 5$) for $t \leq 0.5$. It is noteworthy that the effect of depth ratio h_2/h_1 enters in (4.2) and (4.3) solely through use of c_{00} in definition of the dimensionless time when the Boussinesq approximation is invoked. That is,

$$\frac{\mathcal{W}}{k_s} = \frac{\rho_1 h_2 + \rho_2 h_1}{\rho_2 h_1} \frac{c_{00}^2 h_1}{u_{*0}^2 L} \Rightarrow \frac{c_{0*} h_1}{u_{*0}^2 L} = \mathcal{W}_* \quad (4.5)$$

in the Boussinesq approximation. This reveals, perhaps, a preference for use of \mathcal{W}_* in place of \mathcal{W} , and such a preference is widely exercised (cf. Imberger & Patterson 1990; Horn *et al.* 2001, 2002, etc.). However, with the ratio h_2/h_1 implicit in the scaling for the time t , we prefer in this work to use the more general non-Boussinesq form, as in the derivation of (2.1), throughout this presentation. Recovery of the Boussinesq limit is straightforward from the general forms that follow.

4.3. Effect of wind stress duration

The previous results correspond to a wind forcing that is sustained for a fixed time of $t_0 = 1/4$. Increasing the duration of wind forcing is nominally expected to increase the energy in the wave field. However, the internal response of the lake, including nonlinear effects, can impose a competing effect counteracting the continued steepening of the interface. Figure 5 shows the maximum value of E_2 for various durations (t_0) of a uniform wind stress with $\mathcal{W} = 1$ and $C_f = 0.0025$. The energy input is normalized by that received after a forcing time of $t_0 = 1/4$. The energy gain increases with the

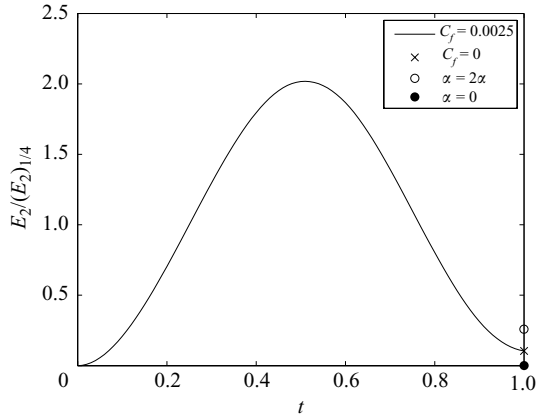


FIGURE 5. Energy input to the internal wave field as a function of the wind-forcing duration for a uniform wind stress with $\mathcal{W} = 1$. Energy is scaled by its value at $t = 1/4$.

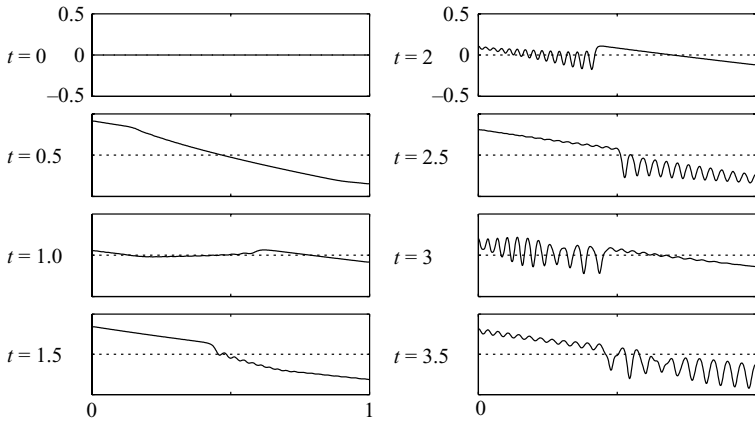


FIGURE 6. Internal wave evolution under sustained uniform wind blowing to the right.

forcing duration until a time of $t_0 = 1/2$. At this time the energy deposited into the internal wave field is maximum, and the internal lake response decreases as the stress is continually applied.

Included in figure 5 are several data points at the time $t = 1$. First, the energy input was also computed with $C_f = 0$ and, as noted by the corresponding data point at $t = 1$, the energy level is imperceptibly changed from the value with $C_f = 0.0025$. This argues for the fact that the non-zero energy at $t = 1$ is due to nonlinear effects. To this point, the energy was computed again for two different cases: one with $\alpha = 0$ in (2.4) and another with the value replaced by 2α in (2.4). Data points from these simulations are shown in figure 5, confirming conclusively that the residual energy after one linear seiche period is determined by nonlinear effects. Nonlinear steepening begins to distort the interface shortly after the time the upwelling–downwelling fronts meet at the lake centre at $t = 1/4$. The evolving linear balance between the baroclinic pressure gradient and the applied wind stress begins to fail after $t \simeq 1/4$ and nonlinearity begins to assert a controlling influence on the dynamics, at least for Wedderburn numbers in the range, say, $1 \leq \mathcal{W} \leq 5$.

The corresponding internal dynamics under sustained wind are shown in figure 6, where selected snap shots of the interface surface displacement for sustained

rightwards wind forcing are presented. The surface is tilted down leeward for $0 < t < 1/2$, but it returns towards the equilibrium line for $1/2 < t < 1$. The return of the surface is caused by the natural free mode seiche. This seesaw-like motion repeats approximately with a seiche period. As exhibited in figure 6, a nonlinear front gradually steepens, and eventually evolves into a train of solitary waves (ISWs). The ISW wavetrain spreads, and goes back and forth, in the domain without significant gain in wave energy (see figure 6 at $t=2$ through $t=3$). After $t=3.5$ the wave field is filled by the shorter wavelength scales of ISWs, and the wave field becomes significantly more complex as the different wave components can not separate in the closed domain. A simulation with sustained forcing for $0 \leq t \leq 20$ revealed that the seiching is damped in the presence of an unsteady wave field that persists throughout the domain.

In order to characterize the significance of the nonlinearity, we define a shock formation time t_s by the relation

$$r = \frac{\left| \frac{\partial f_p}{\partial x}(x, t_s) \right|_{\max}}{\left| \frac{\partial f_p}{\partial x}(x, t_0) \right|_{\max}}. \quad (4.6)$$

The parameter r is a normalized measure of the maximum gradient of the interface. As time increases, the gradient ratio ($|\partial f_p(x, t)/\partial x|_{\max}/|\partial f_p(x, t_0)/\partial x|_{\max}$) increases due to the nonlinear steepening of the wavefront. When the gradient ratio is sufficiently large, a packet of ISWs begins to emerge from the front. We refer, for convenience, to the evolved wavefront as a 'shock' and quite arbitrarily take $r = 10$ for convention as criterion for the formation of a shock. That is, we suppose a shock has formed when the maximum steepness has increased tenfold following cessation of the applied wind stress at $t = t_0$.

One can, of course, define a breaking time obtained by applying the method of characteristics to the nonlinear non-dispersive limit of the unforced non-dispersive version of (2.1). Considering the negative volume (i.e. downwelled portion of the interface on the leeward end immediately following cessation of an applied wind stress) as an isolated initial condition on a semi-infinite domain when $h_2 > h_1$, the breaking time t_B is computed to be

$$t_B = - \left[c_0 \left(\alpha \frac{d\zeta}{dx} + \alpha_2 \frac{d\zeta^2}{dx} \right)_{\max} \right]^{-1}. \quad (4.7)$$

For a uniform wind stress at $t \leq 1/2$, the slope of the interface is (essentially) constant with the value $2\zeta(0, t)/L$. Limiting the model to include only the quadratic nonlinear term (i.e. $\alpha_2 = 0$), this leads to the breaking time estimate presented by Horn *et al.* (2001). However, for more general wind stress distributions, the estimate of t_B is not readily related to the peak upwelling amplitude. Furthermore, when h_2 approaches h_1 from above, the coefficient α_1 tends towards zero and the breaking time depends on both α_2 and the maximum value of the quantity $d\zeta^2/dx$. For these reasons, we prefer to employ the shock formation time given in (4.6).

Figure 7 shows the shock formation time for various \mathcal{W}^{-1} and layer depth ratios with a fixed $h_1/L = 0.002$ and $C_f = 0.0025$. As expected from above discussions, the shock is formed earlier for larger \mathcal{W}^{-1} and deeper lower layers. Also, a longer wind-forcing duration generates the shock earlier, so long as $t_0 \leq 1/2$. As $h_1 \rightarrow h_2$, the leading nonlinear coefficient α , as noted, approaches zero and the shock is not formed

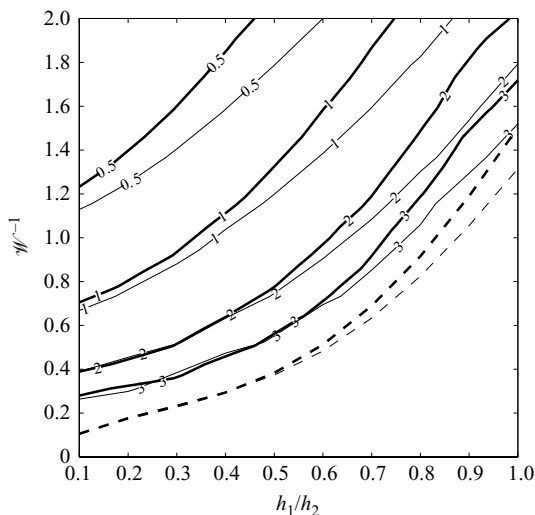


FIGURE 7. Shock formation time ($t_s - t_0$) as a function of inverse Wedderburn number \mathcal{W}^{-1} and the layer depth ratio h_1/h_2 . Bold lines and thin lines represent the forcing duration $t_0 = 1/4$ and $t_0 = 3/8$, respectively. On dashed lines, no shock is formed during four seiche periods after the wind is turned off.

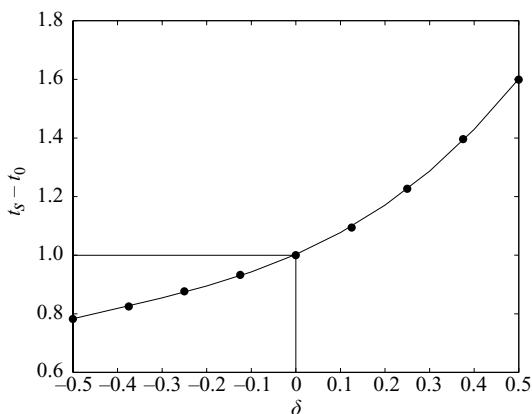


FIGURE 8. Shock formation time ($t_s - t_0$) as a function of spatial gradient δ of wind stress (wind stress function is defined as $X(x) = 1 + \delta(1 - 2x)$). The wind-forcing duration is $t_0 = 1/4$ with strength $\mathcal{W} = 1$. Values are normalized by the value at the uniform stress distribution ($\delta = 0$).

unless the cubic nonlinear term is included in the model. Figure 7 shows a finite shock formation time for $h_1 \approx h_2$ due to the effect of the cubic nonlinearity in the model (2.4).

To understand somewhat the role of wind stress distribution on the shock formation time, we computed the value of $(t_s - t_0)$ defined by (4.6) with $r = 10$ for linearly varying distributions of wind stress. Results are shown in figure 8 as a function of δ , the spatial gradient of the wind stress. When $\delta < 0$, larger wind stress at the leeward end drives a larger downwelled amplitude and steeper interface, leading to an accelerated shock formation. The opposite occurs for $\delta > 0$ with the wind stress increasing towards the windward end.

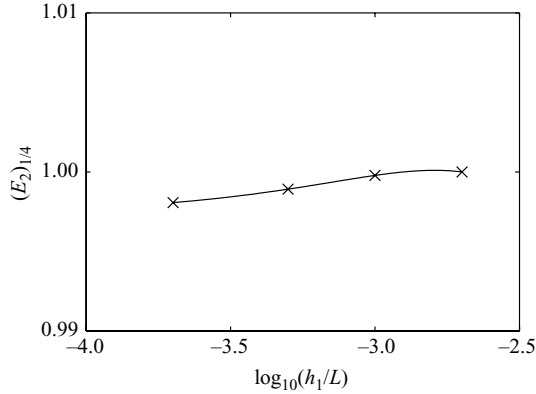


FIGURE 9. Energy computed at $t_0 = 1/4$ as a function of the upper layer aspect ratio h_1/L . Energies are scaled by the value at $h_1/L = 0.002$.

4.4. Effect of layer aspect ratio

The upper layer aspect ratio h_1/L scales only the dispersive and bottom friction terms in the non-dimensional version of the modified KdV model (2.4). As the length of the lake increases, the strength of dispersive effects diminish. Here the aspect ratio determines the length scale of (solitary) waves with respect to the lake length. Our numerical simulation showed that the actual wavelengths for different aspect ratios with the same layer thicknesses were approximately the same, an expected result since the controlling dimension in long wave theory is the smallest layer depth. The longer the length of the lake, the greater the area over which bottom friction acts, although the magnitude of the frictional damping is usually small. In figure 9, we compared the field energies E_2 for different h_1/L with a layer depth ratio $h_1/h_2 = 1/5$ and a uniform wind stress with $\mathcal{W} = 1$. The energy increased slightly for shorter lake length, but the increment is less than 0.3% for change of h_1/L by factor of 10. This slight change in energy is caused by the bottom friction that is scaled by $(h_1/L)^{-1}$. The scaled energies for various forcing durations are imperceptibly changed from that shown in figure 5 for this range of the aspect ratio h_1/L . If the upper layer thickness is the same, the energy input from wind is proportional to the length of the lake for fixed h_1/h_2 . With the observations made in the previous section, the energy input profile (figure 5) is essentially universal for h_1/h_2 , h_1/L and \mathcal{W} .

4.5. Effect of temporal wind stress variations and internal wave resonance

We study in this section the role of different temporal variations of the wind stress on the energy deposition to the internal wave field in a closed basin. Since the model possesses a distinct free-mode natural frequency, it is expected that the wave field possibly becomes resonant if the period of the wind forcing is close to the natural frequency. Thorpe (1974) noted that the large-amplitude internal wave observed in Loch Ness is possibly caused by resonance to periodic wind forcing. To study such internal wave resonance, we set up a periodic unit-pulse wind stress input function as shown in figure 10(a). Each pulse is positive and one-sided (wind blows from left to right) with bandwidth T_0 , and the period of the pulse is T_w .

To demonstrate internal resonance, we let T_w be equal to a seiche period T_s ($=1$), and internal wave evolutions are simulated for $T_0 = 1/4, 1/2, 3/4$ and 1 with a spatially uniform stress, and field energies are calculated for these cases as shown in figure 10(b). The physical parameters were chosen as $h_1/h_2 = 1/5$, $h_1/L = 0.002$ and

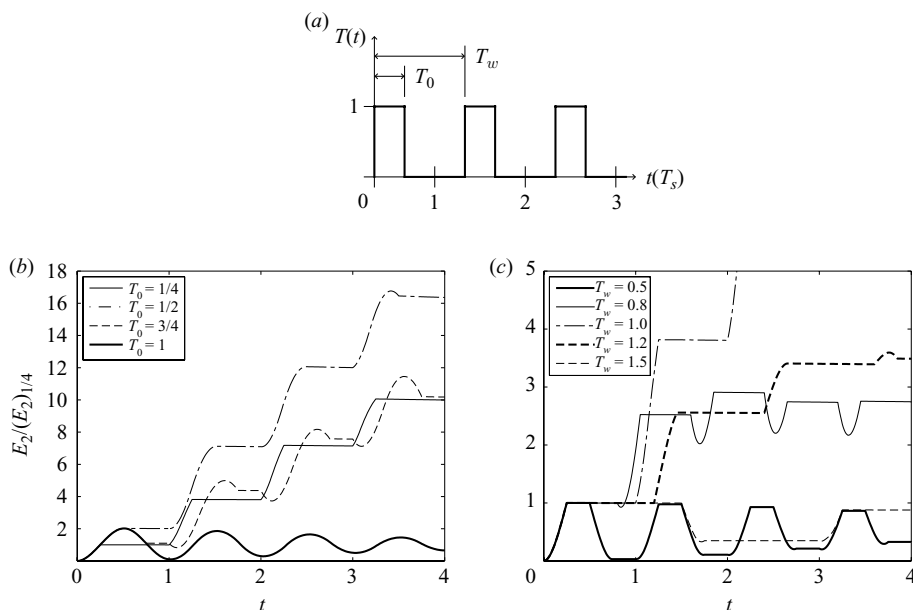


FIGURE 10. (a) Modelled periodic, pulse wind stress input function $T(t)$. Time series of field energies for: (b) different pulse duration T_0 with a fixed forcing period $T_w = T_s$, and (c) different forcing period T_w with a fixed forcing pulse duration $T_0 = 1/4$. Energies in graph (b) are scaled by the value for $T_0 = 1/4$ at $t = 1/4$, and energies in graph (c) are scaled by the value at $t = 1/4$. In all cases $T_s = 1$.

$\mathcal{W} = 1$. For $T_0 = 1/4, 1/2$ and $3/4$, the energy increases after every pulse input. In the present case the bottom boundary loss is so small that the increased energy is not damped effectively. Although it is not shown in this report, the interfacial surface displacement for these input functions shows that the amplitudes of the waves become larger after each wind event. The field energy becomes the highest with $T_0 = 1/2$, and further increase in the pulse duration decreases the input energy because of the reaction of the free mode seiche. For continuous stress input ($T_0 = 1$), the energy rather oscillates with the seiche period, and amplitudes of the oscillations decrease for large t . For large t , the internal seiche is damped, and the unsteady, short waves overwhelm the domain. Although the amplitudes diminish in time due to the damping of the internal seiche, the average energy for each seiche period is approximately the same.

The field energies increase when the wind forcing and internal seiche are in-phase, and vice versa when the forcing and seiche are out-of-phase. Here, ‘in-phase’ is when the interfacial surface is tilting down on the leeward side, and ‘out-of-phase’ is when the surface is tilting up on the leeward side during wind forcing. If the wind forcing and seiche are in phase periodically, the internal wave field becomes resonant as demonstrated above. If in-phase and out-of-phase forcing are repeated one after another, the wave field is expected to be neutral energetically (one particular case is the sustained wind forcing discussed above). Figure 10(c) shows time series of internal wave energies for different forcing periods T_w . For $T_w = 1/2$ and $3/2$, energies oscillate in time because these forcing periods repeat in-phase and out-of-phase forcing periodically, while the energy rapidly increases for the resonant case ($T_w = 1$). For the intermediate cases ($T_w = 0.8$ and 1.2), the energies do not continuously increase as

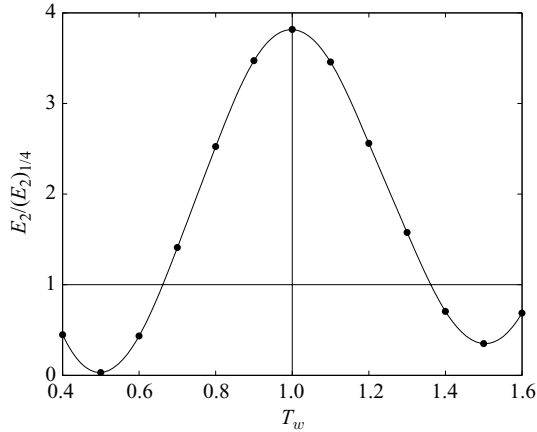


FIGURE 11. Energy gain as a function of forcing period T_w for $T_0 = 1/4$.

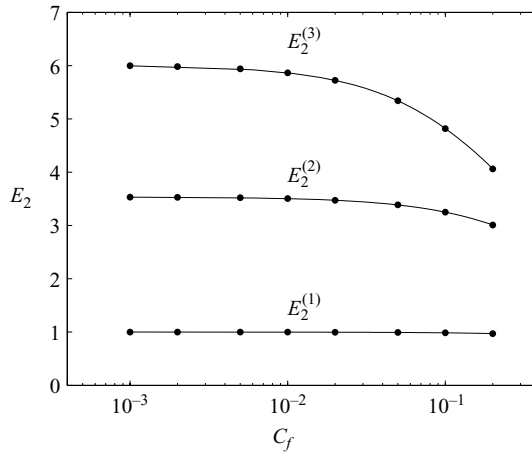


FIGURE 12. First three onset energies during periodic forcing with $T_0 = 1/2$ and $T_w = 1$ as functions of the bottom friction coefficient C_f . Energy values are normalized by the first onset energy $E_2^{(1)}$ with zero bottom friction $C_f = 0$.

the resonant cases, but energies increase for the first three consecutive wind-forcing events. Here, we denote the initial energy level after the first wind forcing as $E^{(1)}$, and so for the next energy level after the second forcing as $E^{(2)}$. Figure 11 shows the energy gain $E^{(2)}/E^{(1)}$ for various forcing periods. The energy gain has a maximum value about 4 at $T_w = 1$ and minima at $T_w = 1/2$ and $3/2$. The energy grows after two consecutive wind pulses ($E^{(2)}/E^{(1)} > 1$), if the wind-forcing period is approximately $0.7 < T_w < 1.3$.

To explore the role of damping on resonant forcing, the energy levels $E_2^{(n)}$ were computed as a function of the bottom friction coefficient for a particular forcing having $T_0 = 1/2$ and $T_w = 1$. The results are presented in figure 12 showing that the higher energy levels are progressively affected by bottom friction, but that even $E_2^{(3)}$ is only marginally affected for values of $C_f \leq 0.0025$.

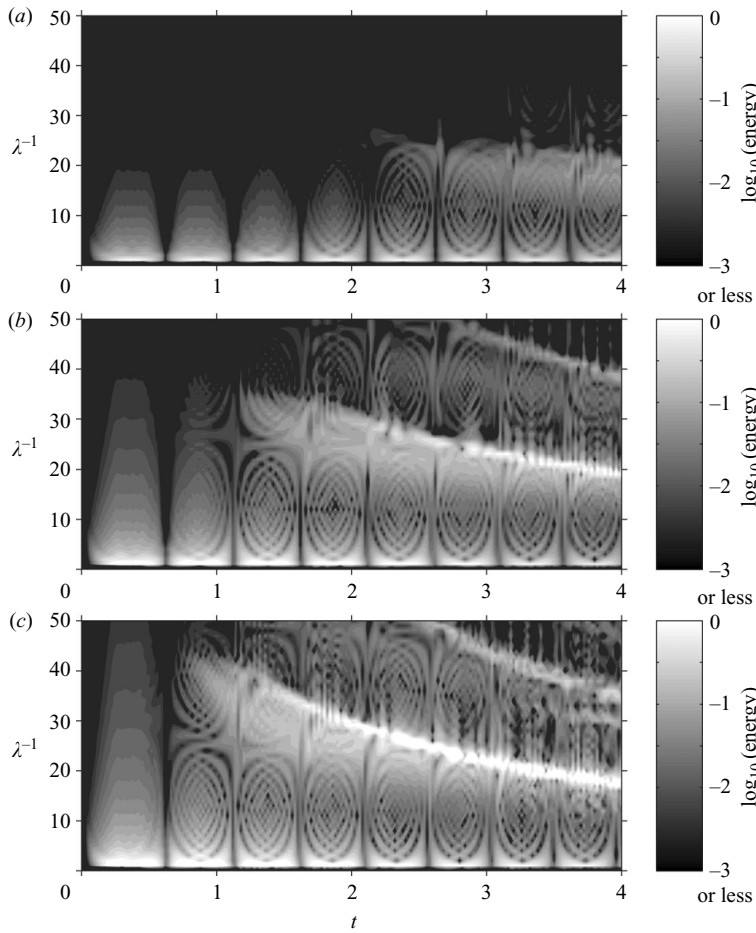


FIGURE 13. Wavenumber spectra of interface displacement f_p as a function of time for Wedderburn numbers (a) $W^{-1} = 0.5$, (b) $W^{-1} = 1$ and (c) $W^{-1} = 1.5$. The wavelength λ is scaled by L . A uniform wind stress is applied for $0 \leq t \leq 1/4$.

5. Downscaling of energy spectra

In order to quantify the energy downscaling from the basin-scale to smaller scales, the time evolution of the wave spectra of the interface displacement $f_p (= \zeta_p / h_1)$ was computed. Figure 13 shows spectral evolutions obtained from numerical simulations with different W^{-1} . The physical parameters were chosen as $h_1/h_2 = 1/5$ and $h_1/L = 0.002$, and a uniform wind stress was applied for a quarter seiche period. Low-wavenumber basin-scale waves dominate the energy spectrum for the early stages after a wind event. Energy flow into higher wavenumber scales becomes apparent approximately at the same time that the nonlinearity, in the presence of very weak dispersion, causes a shock front to form. Subsequently, as ISWs evolve from this front, shorter scale waves spread over the basin due to the influence of dispersion. The influence of dispersion in the wave spectra is manifested as a gradual decrease of wavenumber in the higher wavenumber band that is associated with shocks and ISWs. In figure 14, we computed (a) the total wave energy by integrating the spectra over entire wavenumber range; (b) the energy contained in the basin-scale seiche by

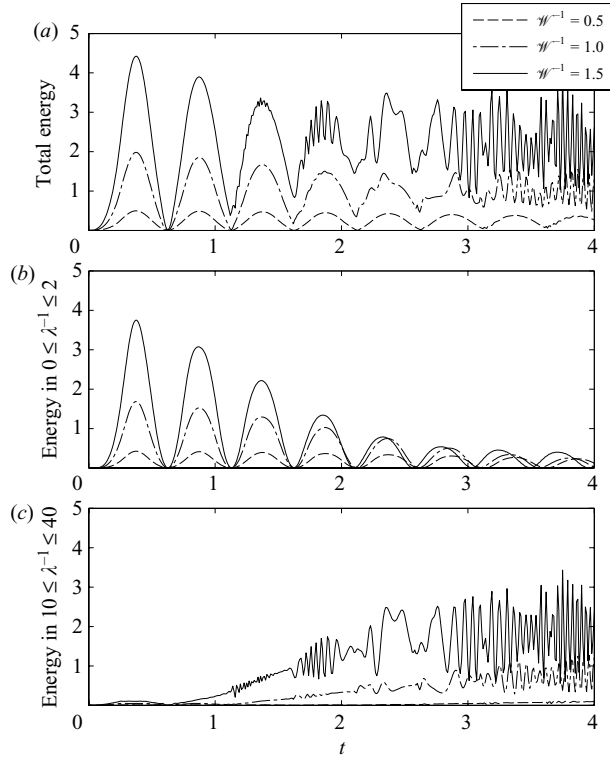


FIGURE 14. Time series of (a) total spectral energy, (b) energy contained in $0 \leq \lambda^{-1} \leq 2$ and (c) energy contained in $10 \leq \lambda^{-1} \leq 40$ for different Wedderburn numbers \mathcal{W} . Energies are scaled by the value for $\mathcal{W} = 1$ at $t = 1/4$.

integrating over the wavenumber band $0 \leq \lambda^{-1} \leq 2$ and (c) the energy contained in shocks and ISWs which is apportioned to the wavenumber band about $10 \leq \lambda^{-1} \leq 40$, where λ is the wavelength scaled by L . The total energy employed here is different from E_2 in previous sections (i.e. E_2 is proportional to the sum of kinetic and potential energy of the flow field as shown in Appendix, but the total energy computed here is proportional only to potential energy). The total energy oscillates in the early stage due to seiching. As ISWs evolve, high-frequency oscillations emerge due to formation of short-scale standing waves arising during reflection of ISWs from the endwalls. The larger the imposed wind stress, the greater the total energy deposited into the low-wavenumber band, which then flows into the nonlinear wave energy band. Again as shown in figure 14, basin-scale motion contains most of the total energy during the early stage, but it decreases gradually as nonlinear waves appear in the evolution process following front formation and subsequent action of dispersion.

6. Effects of variable topography and width

In this section, we first apply the modified KdV model as described by (2.1) for variable topographies. In order to study the effects of the variable topographies, we set up a simple sloping topography model as sketched in figure 15. The basin is the deepest at the left endwall with $h_2 = 5h_1$. The topography possesses a long slope with a height h_b in the middle of the domain, and it is connected to flat

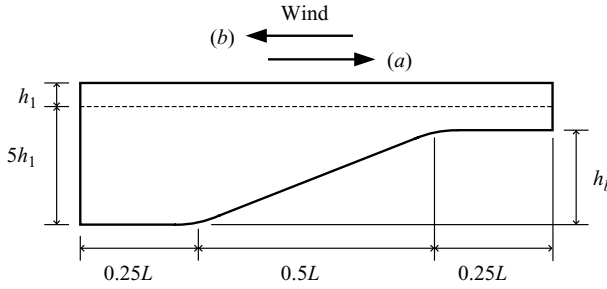


FIGURE 15. Sloping topography set-up for the numerical simulation. The wind stress is applied in either (a) upslope or (b) downslope direction.

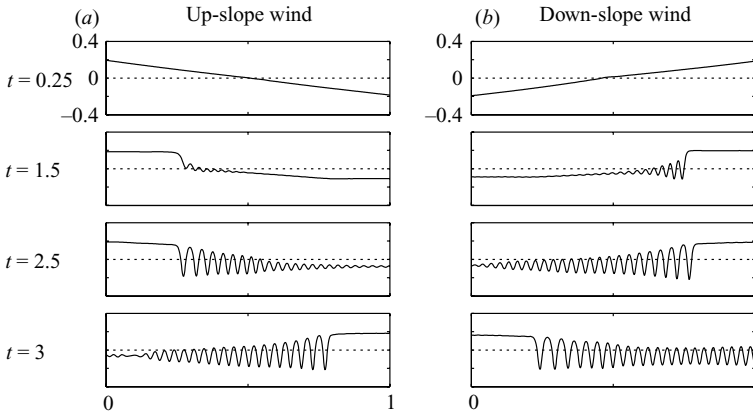


FIGURE 16. Internal wave evolution over the sloping topography with $h_b = 3h_1$ for upslope wind (a), and downslope wind (b). A uniform wind stress with $\mathcal{W} = 1$ is applied for $0 \leq t \leq 1/4$.

surfaces. The slope and flat level surfaces are connected by a smooth curve in order to avoid unphysical numerical noises which are usually caused by topographical discontinuities. The basin width is set to constant, and the upper layer aspect ratio is fixed $h_1/L = 0.002$. The wind stress distribution is fixed uniform. Since the topography is asymmetric, the dynamical responses associated with wind-forcing directions are expected to be different. Figure 16 shows the internal wave evolutions for upslope and downslope wind directions with $\mathcal{W} = 1$. It can be observed that a packet of ISWs appears earlier for the downslope wind than for the upslope wind. Figure 17 shows the shock formation time for various h_b . From figure 17, the difference in the shock formation time increases as h_b increases. When the wind blows in the upslope direction, the wavefront is initiated at the shallower end, where the surface depression (or gradient of the wavefront) is restricted by the shallow water effect (i.e. the coefficient k_s scaling the rate of wind energy input in the evolution equation (2.1) is proportional to h_2 for sufficiently small h_2). The amplitude of the front is being diminished as the front advances in the downslope direction. On the contrary, when the wind blows in the downslope direction, the wavefront is initiated at the deeper end, and the front advances in upslope direction, where the front is amplified. Consequently, as the slope becomes high, the nonlinear effects (shock, ISWs) appear earlier for the downslope wind.

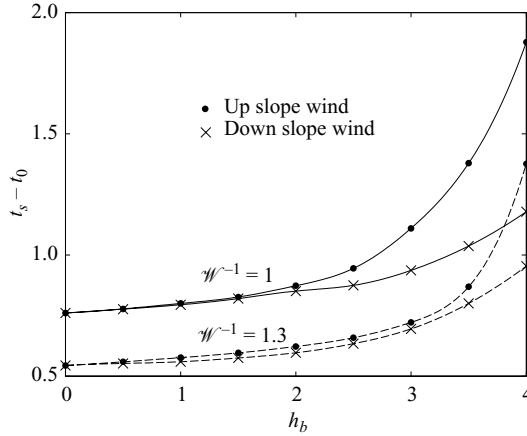


FIGURE 17. Shock formation time ($t_s - t_0$) as a function of the slope height h_b . The wind-forcing duration is $t_0 = 1/4$.

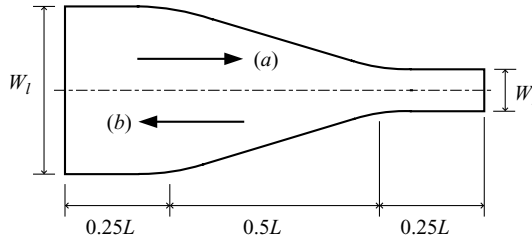


FIGURE 18. Variable width set-up for numerical simulation. Depth is constant ($h_2 = 5h_1$). Wind stress is applied in either (a) narrow end downwind or (b) wide end downwind direction.

To study the effects of variable width we set up a simple geometry as sketched in figure 18. The basin has a greater width W_l on the left section and a narrower width W_r on the right section, and these sections are connected by a smoothly blended straight taper section. We fix $h_1/h_2 = 1/5$, $h_1/L = 0.002$, and use a uniform wind stress distribution. Since the depth is set uniform, all the coefficients in (2.1) are constant. Similar to the variable topography case, we apply the wind stress towards either the narrow end or the wide end. Internal wave evolutions for each wind direction are compared in figure 19. Shock formation and emergence of a train of ISWs appear earlier for wind blowing towards the wide end than for wind blowing towards the narrow end. Differences in the shock formation time increase for higher contraction ratios as shown in figure 20. The reason for the difference is similar to that for the variable topography case. If the wind blows towards the wide end, the wave front is initiated at the wide end, and it advances towards the narrow end where the wavefront is amplified. If the wind blows towards the narrow end, the wavefront is initiated at the narrow end, and it advances towards the wide end where the amplitude of the front is diminished. As the result, the nonlinear shock emerges earlier for a wide end downwind than for a narrow end downwind.

Figure 21 shows temporal signal of the interface surface displacement at $x = 1/4$ and $x = 3/4$ during the time range the wave packet is propagating: (a) in the upslope direction over a variable topography case with $h_b = 3h_1$, and (b) in the narrowing

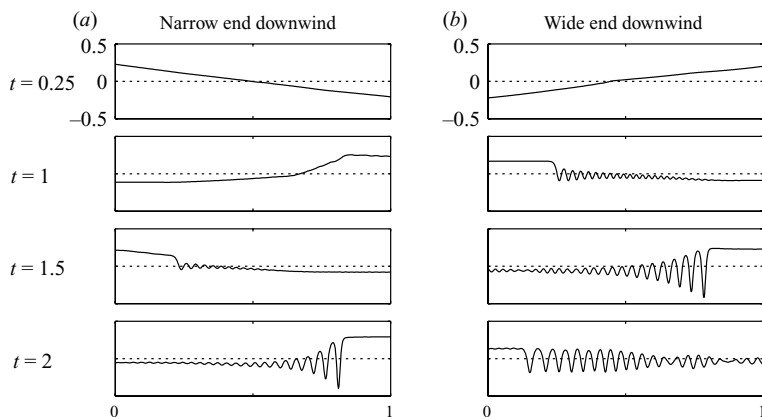


FIGURE 19. Internal wave evolution through variable channel width with $W_r/W_l = 1/3$ for narrow end downwind (a) and wide end downwind (b).

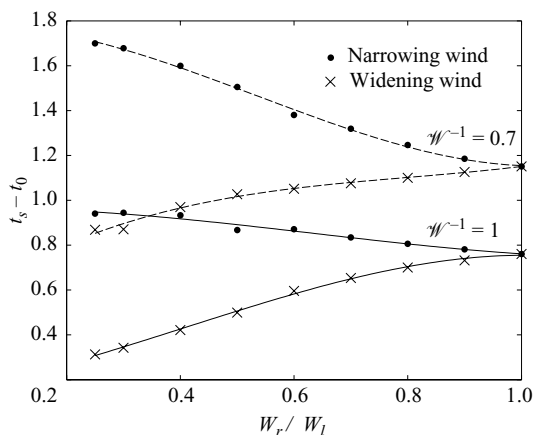


FIGURE 20. Shock formation time ($t_s - t_0$) as a function of the contraction ratio W_r/W_l . The wind-forcing duration is $t_0 = 1/4$.

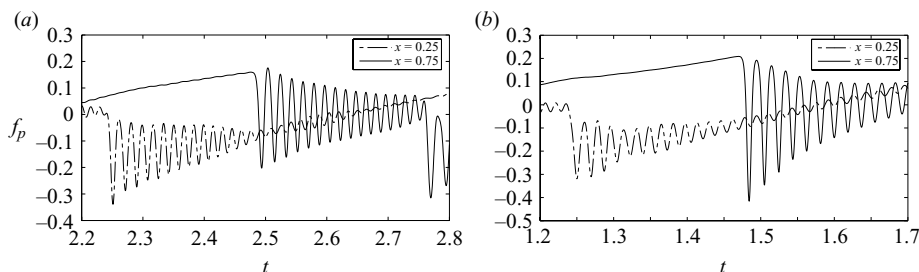


FIGURE 21. Comparison of temporal signal of the interface displacement f_p sampled at $x = 1/4$ and $x = 3/4$ for (a) sloping topography case with $h_b = 3h_1$ and (b) variable width case with $W_r/W_l = 1/3$. In all cases a uniform wind stress with $\mathcal{W} = 1$ is applied for $0 \leq t \leq 1/4$.

direction in a variable width case with $W_r/W_l = 1/3$. These sample points correspond to the beginning and the end points of the sloping bottom or the variable width. It is observed that the wave packet is amplified for both cases. It can be shown that the wave amplitudes are, in turn, diminished when the wave packet is propagating

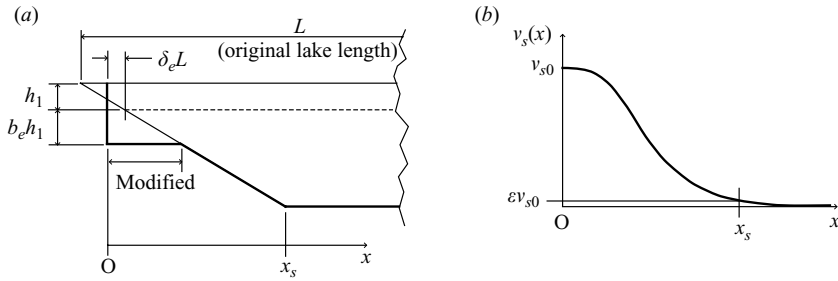


FIGURE 22. (a) Modification of the sloping boundary and (b) schematic of the eddy viscosity function ν_s defined along the modified slope.

in the opposite direction. From the figure the wave amplification ratio is about 1.1 for the variable topography case and about 2.0 for the variable width case. Although contraction ratios of the basin section area are of similar magnitude, the wave amplification of the variable width case is considerably larger than that of the variable topography case. This implies that the amplitudes of the wave packet are effectively amplified (or diminished) through a channel having variable width rather than having variable depth, a result attributable primarily to the fact that the nonlinear coefficient α_1 diminishes with shallower depth h_2 , but α_1 remains unchanged as the width varies.

7. Modelling of reflection and dissipation during shoaling on sloping boundaries

In many stratified lakes the thermocline intersects the sloping boundary at the ends of a basin. Field observations and laboratory experiments have suggested that, when the wind generated internal wave front reflects from the sloping boundary, a significant fraction of its energy is dissipated due to strong mixing at the boundary. This mixing process has an important implication for biological productivity in aquatic systems (Ostrovsky *et al.* 1996). In this section we attempt to apply the KdV-type model to narrow basins with a sloping endwall. First, we propose a geometrical modification to the sloping boundary and, second, introduce an additional dissipation which accounts for the strong dissipation on the slope. This modified model is then compared with the results obtained from experiments.

7.1. Modelling

The theoretical model we used in previous sections is only applicable to lakes where the metalimnion intersects the end at a vertical wall, and waves are assumed to undergo complete reflection at the walls. Since the lower layer depth approaches zero at a sloping boundary, the wave phase speed also approaches zero. Then the wave is 'choked' at the boundary, invalidating a basic premise in the derivation of the KdV model. To prevent the wave choking and yet allow for inclusion of rudimentary aspects of wave shoaling, we introduce a modified geometry to represent a fully sloping boundary. In figure 22(a) we introduce a shelf region with depth $b_e h_1$, where b_e is a free parameter. A vertical wall is placed at the end of the shelf a distance $\delta_e L$ beyond the point of intersection between an equilibrium interface and the sloping bottom. δ_e is a second free parameter, and it is inserted to adjust the phase of the seiche and resulting shock formation. Since the modified domain has vertical endwalls, we can extend the modified domain to the computational domain (figure 2). In order

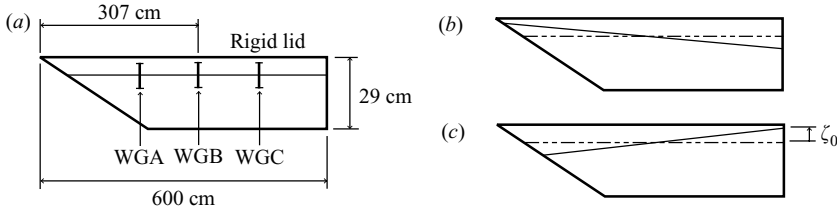


FIGURE 23. (a) Dimension of the laboratory tank. The tank is 30 cm wide uniformly. Three wave gauges (WGA, WGB, WGC) are installed to measure the interface surface displacement. (b) Initial interface surface tilt with upwelling at the slope. (c) Initial interface surface tilt with downwelling at slope. All these figures are not to scale.

to account for the dissipation coming from shear across the metalimnion (interface) and mixing at the sloping boundary, we add a dissipation term that derives rationally if the bulk effect of friction is included in the underlying Boussinesq model. In this case the reduced KdV model has the form

$$\zeta_t + c(\zeta)\zeta_x + \frac{\beta}{2}c_0\zeta_{xxx} + \frac{1}{2}\frac{dc_0}{dx}\zeta = \mathcal{F} - \mathcal{D} + \nu_s\zeta_{xx}. \quad (7.1)$$

The nonlinear terms are now represented by a nonlinear phase speed $c(\zeta)$ function, and ν_s is an eddy viscosity which may depend on space. \mathcal{F} and \mathcal{D} are the wind-forcing and bottom boundary loss terms, respectively, defined in (2.1). It is proposed that the spatial distribution of ν_s be modelled to account for such effects as strong interfacial shear as the wave steepens in the shoaling region, enhanced dissipation as a locally thin bottom layer forms when the interface is drawn towards the sloping boundary (cf. Michallet & Ivey 1999), and energy loss due to wave breaking. Figure 22(b) shows one conceptual distribution of ν_s over the modified domain, assuming its maximum value at the endwall and decreasing to zero over the shoaling region and towards the central portion of the basin.

7.2. Application

Boegman *et al.* (2005a) reported experimental results of long wave packets generated in a closed basin with a sloping boundary. In this section we apply our proposed model to their laboratory tank, and compare our simulation with their experimental results. The laboratory tank is 6 m long, 29 cm ($=H$) deep and 30 cm wide (figure 23a). One endwall is inclined with a slope of either $S = 1/10$ or $S = 3/20$. The other endwall is vertical. The tank is filled with fresh water overlaying saline water, and it is closed by a rigid lid. Before performing an experiment, the tank is rotated to obtain a desired initial tilt of the interface surface. Then at $t = 0$ the tank is rapidly rotated to the horizontal position so that the interface is initially inclined at the original tilt angle of the tank. The initial interface surface is either upwelling or downwelling on the slope (figures 23b and 23c, respectively). Three wave gauges are installed to measure the displacement of interface surface.

Since this experiment corresponds to an initial value problem, the wind-forcing term is turned off. The measured initial interface surface tilt is halved and even-folded onto the computational domain. For direct comparison to experiment, we replace the turbulent bottom friction term by the dissipative effect corresponding to a laminar boundary layer along the surface of the tank (cf. Keulegan 1948; Miles 1976). The

Run	S	h_1/H	ζ_0/h_1	δ_e	ν_{s0} (m ² s ⁻¹)
2	3/20	0.18	-0.86	0.0	0.04
12	3/20	0.20	+0.85	0.07	0.04
20	1/10	0.20	-0.77	0.0	0.002
28	1/10	0.20	+0.58	0.02	0.002

TABLE 1. Parameters of the experimental runs. The density difference was set as $\Delta\rho \approx 20 \text{ kg m}^{-3}$ for all runs. The maximum initial surface displacement ζ_0 is measured at the vertical endwall with a plus(+) or a minus(-) sign to distinguish ζ_0 is either above(+) or below(-) the equilibrium interface surface. Physical wave data from Boegman *et al.* (2005a).

model equation employed here is then given as

$$\zeta_t + c(\zeta)\zeta_x + \frac{\beta}{2}c_0\zeta_{xxx} + \frac{1}{2}\frac{dc_0}{dx}\zeta = \nu_s(x)\zeta_{xx} + \frac{1}{4\pi}\sqrt{\frac{c_0v}{2}}\frac{h_1h_2}{\rho_1h_2 + \rho_2h_1} \times \left\{ \frac{\rho_2}{h_2^2} \left(1 + \frac{2h_2}{b}\right) + \frac{\rho_1}{h_1^2} \left(1 + \frac{2h_1}{b}\right) \right\} \int_{-\infty}^{\infty} |k|^{\frac{1}{2}}(-1 + i \operatorname{sgn}k)\widehat{\zeta}(k, t)e^{ikx} dk, \quad (7.2)$$

where ν , b and $\widehat{\zeta}(k, t)$ are kinetic viscosity, width of the tank and Fourier transform of $\zeta(x, t)$, respectively. Since the wave amplitude in this study, and especially in the shoaling region, is relatively large, we employ a fully nonlinear phase velocity (cf. Ostrovsky & Stepanyants 2005; Sakai & Redekopp 2007):

$$c(\zeta) = c_0 \left[1 + 3\frac{(h_1 - h_2)(h_1 - h_2 - 2\zeta)}{(h_1 + h_2)^2} \times \left(\sqrt{\frac{(h_1 - \zeta)(h_2 + \zeta)}{h_1h_2}} - \frac{h_2 - h_1 + 2\zeta}{h_2 - h_1} \right) \right]. \quad (7.3)$$

Although expressions for the nonlinear, higher order dispersive term are also available (see Koop & Butler 1981; Ostrovsky & Grue 2003), we continued to use only the weakly dispersive term. The spatial distribution of the eddy viscosity ν_s is modelled by a Gaussian function of the form

$$\nu_s(x) = \nu_{s0} \exp \left[- \left(\frac{x}{x_s} \sqrt{|\ln \epsilon|} \right)^2 \right], \quad (7.4)$$

where ϵ is a small fraction of the eddy viscosity at the end of the slope $x = x_s$ (figure 22). We fixed $\epsilon = 0.01$ for all simulations and ν_{s0} was adjusted to yield correspondence with experimental results; i.e. the interface displacement signal obtained at wave gauge B (WGB) so that the reflecting wave packet is properly dissipated after reflection.

We chose four experimental runs for comparison. Parameters for each run are summarized in table 1. It can be shown from (7.3) that, if the amplitude is large, the nonlinear phase velocity may cross zero and become negative for given h_1/h_2 . In such a case the wave can be ‘stagnated’ near the shelf region. The critical amplitude is smaller as the shelf becomes shallower. To avoid this stagnation, the shelf needs to be sufficiently deep. In this study we simply fixed $b_e = 1.5$ for all runs. The shelf extension parameter δ_e was adjusted and determined so that the phase of the wave packet measured at WGB matches the experimental result. The value of δ_e for each run is listed on table 1. Since the domain length is modified in the simulation, the

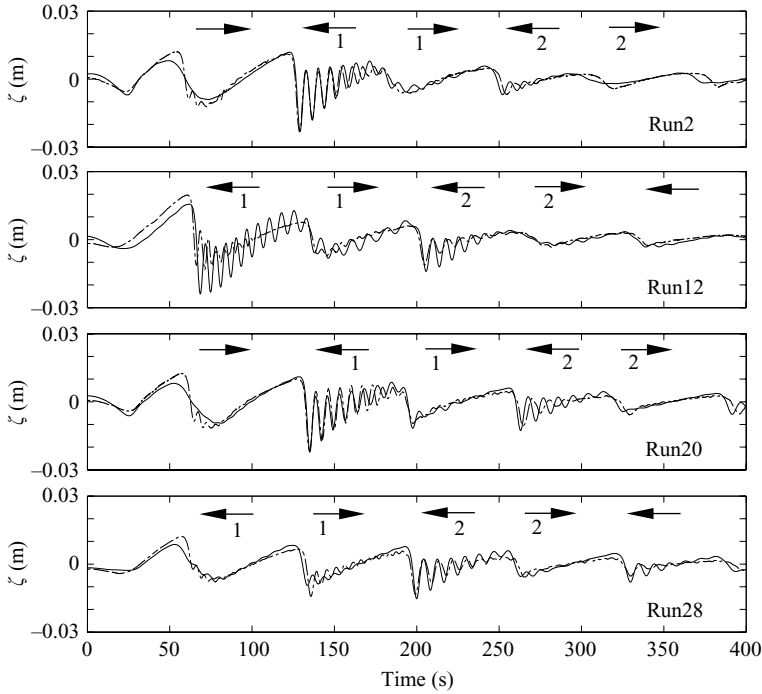


FIGURE 24. Time series of the isopycnal surface displacement ζ_p measured at WGB for Run2, Run12, Run20 and Run28. Solid lines are obtained from the numerical simulations. Dot-dash lines are obtained from the laboratory experiments by Boegman *et al.* (2005a). The wave signals under the left and the right arrows are incoming packet on to the slope and the reflected wave packet from the slope, respectively. The reflection coefficients (see figure 25) are computed for each pair of incoming and reflected wave packet labelled by a number (1 or 2) under each arrow.

initial condition is also modified. In the modified domain, the initial surface slope was kept the same and the position of the interface was adjusted so that the positive and negative volumes are equal. The computational domain was discretized into 512 points, and a time step $\Delta t = 0.0005$ (s) was used for all runs.

Interface displacements measured at WGB are compared in figure 24. For all runs, the phase of the wavefront matches qualitatively for the first and second set of incoming and outgoing packets. For Run2 and Run20 (both are initial conditions with upwelling on the slope), the amplitude of the front during initial reflection is about 20% smaller in the simulation than in the experiment. Since the eddy viscosity was assumed stationary, this was caused by excessive dissipation of the initial wavefront at the slope. In the first incoming packet, about three to five solitons are well predicted by the numerical model. For Run12, the first incoming packet possesses larger amplitude oscillations, and the wave amplitudes significantly deviate from the experiment. The packet is initiated at the vertical endwall where the eddy viscosity is zero. Since the initial amplitude is large ($\zeta_0/h_1 = 0.85$), some additional eddy dissipation may need to be considered. For Run28 where $\zeta_0/h_1 = 0.58$, no such high-amplitude oscillation was observed in the numerical simulation. For Run12 and Run28, by taking account of the resolution of the experimental measurement, which is ± 2 mm, the first two or three major solitons are well predicted by the numerical model (see $200 \leq t \leq 230$ [s]).

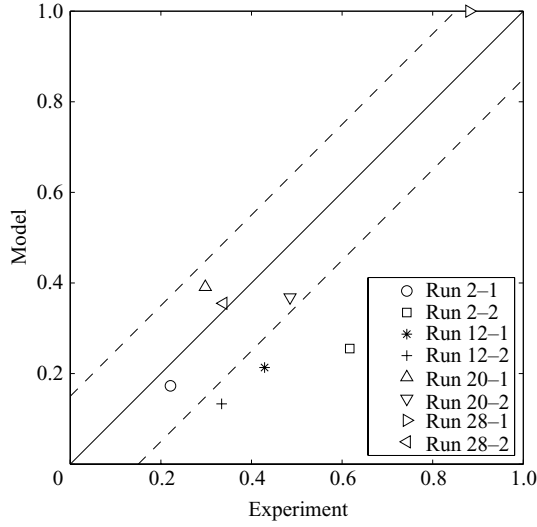


FIGURE 25. Comparison of reflection coefficients E_r/E_i obtained from the laboratory experiments and the numerical model. Dash number in each label indicates the number of reflection as indicated in figure 24. Dash lines are ± 0.15 deviation from the equal line.

We define here a reflection coefficient E_r/E_i as a ratio of the energy of the reflected wave packet over that of the incoming wave packet:

$$\frac{E_r}{E_i} = \frac{1}{t_3 - t_2} \frac{\int_{t_2}^{t_3} \Delta \rho \zeta^2 dt}{\frac{1}{t_2 - t_1} \int_{t_1}^{t_2} \Delta \rho \zeta^2 dt}. \quad (7.5)$$

The interval $[t_1, t_2]$ and $[t_2, t_3]$ are intervals of incoming and reflected packets, respectively. The reflection coefficients for experimental and numerical runs were computed and compared in figure 25. Five out of eight reflection coefficients fall into ± 0.15 deviation range. All reflection coefficients obtained from Run12 numerical simulation are about 50 % smaller than those of the experiment, primarily because the high-amplitude oscillations are not damped at the vertical endwall in the numerical model. Although the first reflection coefficient for Run2 is well predicted by the numerical model, the second reflection coefficient is about 50 % smaller than that of experiment. From figure 25, the numerical model is over damping for the second reflected packet, but at this stage, wave amplitudes are quite small and experimental resolution is comparable to the wave amplitudes. Measured reflection coefficients can vary significantly by such an error.

From table 1, eddy viscosities seem to depend primarily on slope S . An increase in slope by a factor of 1.5 results in an increase in the eddy viscosity by a factor of 100. For large slope ν_s can increase, but the region of slope becomes shorter in the domain. Hence, total dissipation effects are expected to be weaker for larger slopes. The domain extension parameter δ_e had to be adjusted for Run12 and Run28 cases in which initial conditions are both downwelling at slope in order to match the measured shock formation position. Due to the very limited number of experiments for comparison, the functional dependence of δ_e remains open. However, based on available data, we can propose the ‘closed’ shoaling model (7.2) with the model

parameters δ_e and $\nu_{s,0}$ given by

$$\delta_e = \begin{cases} 0, & \frac{\zeta_0}{h_1} < 0.5, \\ \frac{1}{10} \left(2 \frac{\zeta_0}{h_1} - 1 \right), & \frac{\zeta_0}{h_1} > 0.5; \end{cases} \quad (7.6)$$

$$\nu_{s,0} = \frac{1}{2} \nu \exp[(20 \ln 20)S]. \quad (7.7)$$

The values of $\zeta_0 = \zeta(x=0, t)$ can be obtained from relation (4.2) using the relevant Wedderburn number \mathcal{W} and lake depth ratio h_2/h_1 . Better definition of these parameters awaits further experiments of the type reported by Boegman *et al.* (2004).

8. Conclusions

A variable environmental driven-damped KdV-type model was applied to the problem of wind-forced internal wave generation in narrow lakes, and the model was found to be useful for obtaining first-order physical information for various sets of parameters with minimal computational effort. The spatial distribution of the wind stress over the lake surface is an important factor to determine the total energy input to the internal wave field. Even if the integral of the stress distribution is the same, the total energy inputs are quite different as demonstrated by using sinusoidal and uniform wind stress distributions. We were able to also demonstrate an internal wave resonance phenomena. If the wind blowing over a lake surface is near its seiche frequency, it is possible that the wave is amplified and the field energy continues to grow.

Duration of wind forcing is an important factor in predicting the total field energy. Maximum energy is obtained when the wind blows for half a seiche period. Therefore, the wind-forcing frequency and duration of each forcing event are important parameters for studying the dynamical response of lakes. Such dynamical behaviour can be easily simulated by using the present model. We studied effects of key environmental parameters: the layer depth ratio h_1/h_2 , the upper layer aspect ratio h_1/L and Wedderburn number \mathcal{W} . Energy input with respect to the wind-forcing duration appears to be universal. The form of wind energy input curve does not depend on these parameters.

We have quantified the effect of nonlinearity by defining a shock formation time. The shock formation time is well parameterized by using \mathcal{W}^{-1} and h_1/h_2 . We have quantified the energy downscale processes by computing time evolution of wave spectra. It was shown (in figure 14) that the basin-scale energy is continually transferred to shorter length scales (solitary waves). Such shorter length scale waves are generated by the interactions between nonlinear and non-hydrostatic effects in the equations of motion.

The numerical model was applied to variable topography and variable width lake models. Wave amplification during propagation up a slope or into a contraction was well produced by the numerical model. Similar to results for rectangular lakes, basin-scale energy is continually transferred to shorter length scales, but at accelerated rates. Although variable topography introduces spatially varying coefficients in each term in the numerical model, these coefficients are constant for variable width with constant topography. As demonstrated in §6, the variable width is a more effective wave amplifier than the variable depth.

Our numerical model was applied to shoaling along a sloping boundary by introducing a shelf region and by introducing a second-order dissipation term multiplied by an eddy viscosity. It was found to be possible to produce results that match experiments qualitatively. We attempted to reduce the number of free parameters to the maximum eddy viscosity ν_0 and a shelf extension parameter δ . ν_0 appears to be dependent primarily on the slope. Parameterization of δ_e is left unknown. Since this is the first attempt to apply a simple numerical model to shoaling on a sloping boundary, further study of the modelling and parametrization are left for future work.

The authors acknowledge the receipt of helpful comments from anonymous reviewers.

Appendix. Total energy of the flow field

Consider the linear Boussinesq equation for an interfacial wave in a medium with constant depth:

$$\begin{aligned}(h_1 u_1)_t - c_0^2 \zeta_x &= 0, \\ \zeta_t - (h_1 u_1)_x &= 0.\end{aligned}$$

From these equations, we can construct the conservation equation

$$\frac{\partial}{\partial t} \left\{ \frac{h_1^2 u_1^2 + c_0^2 \zeta^2}{2} \right\} + \frac{\partial}{\partial x} \{ -c_0^2 h_1 u_1 \zeta \} = 0. \quad (\text{A } 1)$$

An equation of similar form exists for the lower layer. Adding the equations for the separate layers yields

$$\frac{\partial}{\partial t} \left\{ \frac{h_1^2 u_1^2 + h_2^2 u_2^2}{2} + c_0^2 \zeta^2 \right\} + \frac{\partial}{\partial x} \{ c_0^2 (h_2 u_2 - h_1 u_1) \zeta \} = 0. \quad (\text{A } 2)$$

The first bracketed term is proportional to the total energy density, which contains horizontal kinetic energy of the fluid in the upper and lower layers and the potential energy resulting from deflection of interfacial surface. The second bracketed term is proportional to the total horizontal momentum flux of the upper and lower layers. Integrating (A 2) over the physical domain $[0, L]$, and using the velocity vanishing boundary condition, we get

$$\frac{\partial}{\partial t} \int_0^L \left\{ \frac{1}{2} (h_1^2 u_1^2 + h_2^2 u_2^2) + c_0^2 \zeta^2 \right\} dx = 0. \quad (\text{A } 3)$$

Using f and g to represent the right- and left-going displacement functions in the extended computational domain (see §2), u_1 , u_2 and ζ can be expressed

$$u_1 = -\frac{c_0}{h_1} (f - g); \quad u_2 = \frac{c_0}{h_2} (f - g); \quad \zeta = f + g. \quad (\text{A } 4)$$

Substituting (A 4) into (A 3), we have

$$\frac{\partial}{\partial t} \int_0^L f^2 + g^2 dx = \frac{\partial}{\partial t} \int_0^{2L} f^2 dx = 0,$$

after using (2.3). Thus, the integral of square of the amplitude over the computational domain is a conserved quantity, which can be interpreted as the total energy of the flow field.

REFERENCES

- BAINES, P. G. 1995 *Topographic Effects in Stratified Flows*. Cambridge University Press.
- BOEGMAN, L., IVEY, G. N. & IMBERGER, J. 2004 An internal solitary wave parameterization for hydrodynamic lake models. In *Proceedings of Fifteenth Australasian Fluid Mechanics Conference*. The University of Sydney, Sydney, Australia.
- BOEGMAN, L., IVEY, G. N. & IMBERGER, J. 2005a The degeneration of internal waves in lakes with sloping topography. *Limnol. Oceanogr.* **50** (5), 1620–1637.
- BOEGMAN, L., IVEY, G. N. & IMBERGER, J. 2005b The energetics of large-scale internal wave degeneration in lakes. *J. Fluid Mech.* **531**, 159–180.
- BOURGAULT, D. & KELLY, D. 2007 On the reflectance of uniform slopes for normally incident interfacial solitary waves. *J. Phys. Oceanogr.* **37**, 1156–1162.
- DRAZIN, P. G. & JOHNSON, R. S. 1989 *Solitons: An Introduction*, pp. 90–95. Cambridge University Press.
- FARMER, D. M. 1978 Observations of long nonlinear internal waves in lake. *J. Phys. Oceanogr.* **8**, 63–73.
- FORNBERG, B. & WHITHAM, G. B. 1978 A numerical and theoretical study of certain nonlinear wave phenomena. *Phil. Trans. R. Soc. Lond. A* **289**, 373–404.
- GARDNER, C. S. 1971 The Korteweg–deVries equation and generalizations. IV. The Korteweg–deVries equation as a Hamiltonian system. *J. Math. Phys.* **12**, 1548–1551.
- GRIMSHAW, R. 2002 *Environmental Stratified Flow*. Kluwer Academic.
- GRIMSHAW, R., PELINOVSKY, E. & TALIPOVA, T. 2007 Modelling internal solitary waves in the coastal ocean. *Surv. Geophys.* **28**, 273–298.
- HEAPS, N. S. 1984 Vertical structure of current in homogeneous and stratified waters. In *Hydrodynamics of Lakes* (ed. K. Hutter), pp. 153–207. Springer Verlag Wien.
- HEAPS, N. S. & RAMSBOTTOM, A. E. 1966 Wind effects on the water in a narrow two-layered lake. *Phil. Trans. R. Soc. Lond. A* **259**, 391–430.
- HELFRICH, K. R. 1992 Internal solitary wave breaking and run-up on a uniform slope. *J. Fluid Mech.* **243**, 133–154.
- HELFRICH, K. R. & MELVILLE, W. K. 2006 Long nonlinear internal waves. *Annu. Rev. Fluid Mech.* **38**, 395–425.
- HORN, D. A., IMBERGER, J. & IVEY, G. N. 2001 The degeneration of large-scale interfacial gravity waves in lakes. *J. Fluid Mech.* **434**, 181–207.
- HORN, D. A., IMBERGER, J., IVEY, G. N. & REDEKOPP, L. G. 2002 A weakly nonlinear model of long internal waves in closed basins. *J. Fluid Mech.* **467**, 269–267.
- HUNKINS, K. & FLIEGEL, M. 1973 Internal undular surges in Seneca lake: a natural occurrence of solitons. *J. Geophys. Res.* **78**, 539–548.
- IMBERGER, J. 1994 Transport processes in lakes: a review. In *Limnology Now: A Paradigm of Planetary Problems* (ed. R. Margalef), pp. 99–193. Elsevier.
- IMBERGER, J. 1998 *Coastal and Estuarine Studies*. American Geophysical Union.
- IMBERGER, J. & PATTERSON, J. C. 1990 Physical limnology. *Adv. Appl. Mech.* **27**, 303–475.
- KEULEGAN, G. H. 1948 Gradual damping of solitary waves. *J. Res. Natl Bur. Stand.* **40**, 487–498.
- KOOP, C. G. & BUTLER, G. 1981 An investigation of internal solitary waves. *J. Fluid Mech.* **112**, 225–251.
- LAMB, K. G. & NGUYEN, V. T. 2009 Calculating energy flux in internal solitary waves with an application to reflectance. *J. Phys. Oceanogr.* **39**, 559–580.
- MICHALLET, H. & IVEY, G. N. 1999 Experiments on mixing due to internal solitary waves. *J. Geophys. Res.* **104** (C6), 13467–13477.
- MILES, J. W. 1976 Damping of weakly nonlinear shallow-water waves. *J. Fluid Mech.* **76**, 251–257.
- MONISMITH, S. 1986 An experimental study of the upwelling response of stratified reservoirs to surface shear stress. *J. Fluid Mech.* **171**, 407–439.
- MORTIMER, C. H. 1952 Water movements in lakes during summer stratification; evidence from the distribution of temperature in Windermere. *Phil. Trans. Roy. Soc. Lond. B* **236**, 355–404.
- OSTROVSKY, L. A. & GRUE, J. 2003 Evolution equations for strongly nonlinear internal waves. *Phys. Fluids* **15**, 2934–2948.
- OSTROVSKY, L. A. & STEPANYANTS, Y. A. 2005 Internal solitons in laboratory experiments: Comparison with theoretical models. *Chaos* **15**, 037111.

- OSTROVSKY, I., YACOBI, Y. Z., WALLINE, P. & KALIKHMAN, I. 1996 Seiche-induced mixing: its impact on lake productivity. *Limnol. Oceanogr.* **41** (2), 323–332.
- SAGGIO, A. & IMBERGER, J. 1998 Internal wave weather in a stratified lake. *Limnol. Oceanogr.* **43**, 1780–1795.
- SAKAI, T. & REDEKOPP, L. G. 2007 Models for strongly-nonlinear evolution of long internal waves in a two-layer stratification. *Nonlinear Process. Geophys.* **14**, 31–47.
- SAKAI, T. & REDEKOPP, L. G. 2009 A weakly nonlinear model for multi-modal evolution of wind-generated long internal waves in a closed basin. *Nonlinear Process. Geophys.* **16**, 487–502.
- STEVENS, C. & IMBERGER, J. 1996 The initial response of a stratified lake to surface shear stress. *J. Fluid Mech.* **312**, 39–66.
- TENG, M. H. & WU, T. Y. 1992 Nonlinear water waves in channels of arbitrary shape. *J. Fluid Mech.* **242**, 211–233.
- THORPE, S. A. 1974 Near-resonant forcing in a shallow two-layer fluid: a model for the internal surge in Loch Ness? *J. Fluid Mech.* **63**, 509–527.
- THORPE, S. A. & HALL, A. 1972 The internal surge in Loch Ness. *Nature* **23**, 96–98.
- THORPE, S. A., KEEN, J. M., JIANG, R. & LEMMIN, U. 1996 High-frequency internal waves in Lake Geneva. *Phil. Trans. R. Soc. Lond. A* **354**, 237–257.
- WIEGAND, R. C. & CARMACK, E. 1986 The climatology of internal waves in deep temperate lake. *J. Geophys. Res.* **91**, 3951–3958.
- WÜEST, A. & LORKE, A. 2003 Small-scale hydrodynamics in lakes. *Annu. Rev. Fluid Mech.* **35**, 373–412.